4D anisotropic skeletal muscle tissue constructs fabricated by staircase effect strategy

Shida Miao[1], **Margaret Nowicki**[2], **Haitao Cui**[1], **Se-Jun Lee**[1], **Xuan Zhou**[1], **David K Mills**[3], **Lijie Grace Zhang**[1,4,5,6]

[1]Department of Aerospace and Mechanical Engineering, The George Washington University, 800 22nd St, NW Washington DC 20052, United States of America

[2]Department of Civil and Mechanical Engineering, The United States Military Academy, West Point, New York, 10996, United States of America

[3]School of Biological Sciences and the Center for Biomedical Engineering & Rehabilitation Science. Louisiana Tech University, Ruston, LA 71272, United States of America

[4]Department of Biomedical Engineering, The George Washington University, 800 22nd St, NW Washington DC 20052, United States of America

[5]Department of Electrical and Computer Engineering, The George Washington University, 800 22nd St, NW Washington DC 20052, United States of America

[6]Department of Medicine, The George Washington University, 2150 Pennsylvania Ave, NW Washington DC 20052, United States of America

Like the morphology of native tissue fiber arrangement (such as skeletal muscle), unidirectional anisotropic scaffolds are highly desired as a means to guide cell behavior in anisotropic tissue engineering. In contrast, contour-like staircases exhibit directional topographical cues and are judged as an inevitable defect of fused deposition modeling (FDM). In this study, we will translate this staircase defect into an effective bioengineering strategy by integrating FDM with surface coating technique (FCT) to investigate the effect of topographical cues on regulating behaviors of human mesenchymal stem cells (hMSCs) toward skeletal muscle tissues. This integrated approach serves to fabricate shape-specific, multiple dimensional, anisotropic scaffolds using different biomaterials. 2D anisotropic scaffolds, first demonstrated with different polycaprolactone concentrations herein, efficiently direct hMSC alignment, especially when the scaffold is immobilized on a support ring. By surface coating the polymer solution inside FDM-printed sacrificial structures, 3D anisotropic scaffolds with thin wall features are developed and used to regulate seeded hMSCs through a self-established rotating bioreactor. Using layer-by-layer coating, along with a shape memory polymer, smart constructs exhibiting shape fix and recovery processes

lgzhang@gwu.edu.

are prepared, bringing this study into the realm of 4D printing. Immunofluorescence staining and real-time quantitative polymerase chain reaction analysis confirm that the topographical cues created via FCT significantly enhance the expression of myogenic genes, including myoblast differentiation protein-1, desmin, and myosin heavy chain-2. We conclude that there are broad application potentials for this FCT strategy in tissue engineering as many tissues and organs, including skeletal muscle, possess highly organized and anisotropic extracellular matrix components.

1. Introduction

Skeletal muscle comprises roughly 60% of the body's average weight and performs many critical functions, including but not limited to control and movement of limbs, respiration, and protection of abdominal viscera [1]. Skeletal muscle tissues possess innate repair potential especially for small lesions and defects, but surgical intervention is often required to prevent scar tissue formation and loss of function when muscle defects are larger than a critical volume and beyond normal physiological repair processes [2]. If the muscular function is impaired or mass tissue loss exceeds 20%, as with muscle wasting diseases such as muscular dystrophy, the lesions are generally designated as volumetric muscle loss [3]. Notably, muscle wasting diseases affect over five million people world-wide, currently presenting and advancing further into a serious societal and economic burden [4].

An autograft of healthy muscle tissue is the current clinical standard for treating serious muscle damage. Surgical grafting such as this has many limitations, such as shortage of donor tissue, loss of function at the donor site and donor-site morbidity [5]. Different alternative strategies have been explored to promote muscle repair and regeneration over the last few decades, including surgical techniques, physical therapy, biomaterials, cell therapy, and muscle tissue engineering [6, 7]. Among the various techniques, skeletal muscle tissue engineering, which involves both biomaterials and cells via valid models and functional constructs, is a promising approach for functional restoration of damaged muscle tissues [8, 9]. Typically, the tissue engineering process involves the design and fabrication of a scaffold that closely mimics the native skeletal-muscle extracellular matrix, promoting the organization of cells into a physiologically relevant architecture [8, 9]. Highly oriented myofibers, composed of multinucleated muscle cells, are densely packed in skeletal muscle tissues. Without proper alignment of myofibers, muscle fibers cannot effectively transmit force and contract efficiently. As such, unidirectional anisotropic scaffolds that mimic the morphology of the native skeletal-muscle arrangement are highly desired as a means to guide cell alignment, elongation, proliferation, and differentiation into myotubes [5].

Various methods have been employed for fabricating anisotropic scaffolds. Electrospinning of natural and/or artificial polymers is a widely applied process to produce aligned nanofibers for inducing organization within cell sheets [10–13]. When cultured on these surfaces, human mesenchymal stem cells (hMSCs) aligned and elongated in both cell morphology and nuclear locations because of the nanometer-scale topographical features [10, 11]. Similarly, anisotropic nano-architectures, assembled by magnetic-field-directed self-assembly, have provided sufficient physical cues to align cells independent of the extra-cellular matrix composition [14]. In addition to nanoscale topography, microgrooves

generated by uniaxially stretching poly (ε-caprolactone) films provided geometric cues to align hMSCs [15–17]. Photolithographic techniques are notably used to pattern microchannels for aligning stem cells, usually using polydimethylsiloxane as the constructing material [18, 19]. Combining 3D techniques with other approaches, such as etching and direct writing, have also been reported as offering great application potential [20, 21]. Interestingly, a photolithographic-stereolithographic-tandem fabrication technique was used to construct 4D smart anisotropic scaffolds for improved stem cell differentiation [22]. This simple, yet efficient, technique was validated by rapid printing of scaffolds with well-defined and consistent micro-surface features where hMSCs actively grew and were highly aligned along the micropatterns, forming an uninterrupted cellular sheet [22]. The 4D dynamic shape change transformed a 2D design into a 3D structure, which may facilitate seamless integration with damaged tissues or organs [22]. Considering the beneficial capabilities of rapid customization, as well as the addition of time-dependent dynamic processes, 3D/4D printing techniques to fabricate smart anisotropic scaffolds might be a favorable trend in the near future.

Fused deposition modeling (FDM) is a sophisticated additive manufacturing technique for fabricating biomedical scaffolds with controlled pore size, morphology, and interconnectivity [23, 24]. Due to the additive nature of this printing process, the thickness of each layer determines the resolution of the printed scaffolds. Lower layer height usually results in structures with smoother surfaces and the typical layer height of FDM is down to 50 μm [25]. The staircase effect, which is caused by the layered manufacturing process, exhibits contour-like surfaces on the printed structures and is an inevitable result seen in FDM fabricated scaffolds; as such, it is sometimes seen as a defect or shortcoming of this process [26]. In order to obtain a smooth structure without surficial staircases, post-polishing procedures are usually performed [26]. However, the contour-like surfaces are anisotropic, which is a desirable characteristic in the field of tissue engineering. Turning this staircase effect into a prominent strategy for developing anisotropic topological cues would be beneficial and provide alternative and unique methods for engineering novel skeletal muscle tissue scaffolds.

In this study, we fabricate shape-specific, four-dimensional, anisotropic scaffolds by integrating the staircase effect of FDM printing with a coating technique (FCT) and investigate the topographical cues for regulating behaviors of growth and differentiation of hMSCs toward the skeletal muscle phenotype. As shown in figure 1, a specific structure with staircase feature is first printed via FDM with a sacrificial material, which will be completely removed after coating with different polymer solutions. After removal of sacrificial material, hMSC behaviors on the scaffold will be regulated and investigated. While FDM printing can already create complex structures for specific tissue engineering requirements, the surface coating technique introduces a thin film feature to the scaffolds, providing an interesting and efficient way for establishing thin film features in three dimensions. The size of the staircases on the FDM printed structures is fully controllable through the layer height parameter, indicating a straightforward approach to manipulating the surface morphology. Additionally, FCT can effortlessly introduce smart materials into the scaffolds in a layer-by-layer pattern, bringing this research into the realm of 4D printing, as illustrated in figure 1(e). The hMSCs' potential toward skeletal muscle tissue

differentiation will be observed and studied using confocal microscopy and reverse transcription polymerase chain reaction (RT-PCR) analysis. Considering that many tissues and organs besides skeletal muscle possess highly organized and anisotropic extracellular matrix components, the FCT strategy in this study is expected to have broad applications in the tissue engineering field.

2. Experimental section

2.1. Chemicals and materials

Polyvinyl alcohol (PVA) filament for 3D printing was obtained from Matter Hackers (Orange County, California). Polycaprolactone (average Mn 80 000) (PCL), poly lactic acid (average Mn 20 000) (PLA), agarose, soybean oil epoxidized acrylate (SOEA) (contains 4000 ppm monomethyl ether hydroquinone as inhibitor), formaldehyde 10% (neutral buffered), dexamethasone, hydrocortisone, chloroform and monoclonal anti-desmin antibody produced in mouse were obtained from Sigma-Aldrich (MO, USA). Goat anti-mouse Alexa Fluor® 488 (IgG H&L) was purchased from Abcam (Cambridge, MA). Bis (2,4,6-trimethylbenzoyl)-phenylphosphineoxide (Ciba Irgacure 819) was purchased from Ciba Specialty Chemicals (Basel, Switzerland). Alpha minimum essential medium (MEM Alpha (1×)+Gluta MAXTM-1), l-glutamine and penicillin/streptomycin solution were obtained from Thermo Fisher Scientific (Waltham, MA). Fetal bovine serum (FBS) was purchased from Gemini Bioproducts (West Sacramento, CA). DAPI (4′,6 - Diamidino - 2 - phenylindole, dihydrochloride) was purchased from Anaspec Inc (Fremont, CA). Phosphate-buffered saline (PBS), without calcium & magnesium, and Trypsin/EDTA (1 × 0.25% Trypsin/2.21 mM ethylenediaminetetraacetic acid (EDTA) in Hank's balanced salt solution without sodium bicarbonate, calcium, and magnesium) were supplied by Mediatech Inc (Manassas, VA). Primary hMSCs were obtained from healthy consenting donors at the Texas A&M Health Science Center, Institute for Regenerative Medicine. Unless otherwise listed, all solvents and reagents were purchased from Aldrich Chemical Co. (St. Louis, MO) and used as received.

2.2. Design and FDM printing of 3D structures

The expected structure was drawn with Autodesk123D software (Autodesk Inc, CA, USA), saved as a stl format file, and loaded into the software Slic3r, which is licensed under the GNU Affero General Public License, version 3. The infill density, the printing speed, and the layer height were assigned in Slic3r. Other typical parameters assigned in Slic3r include: top 0, bottom 0; 90° infill angle, 10 mm^2 solid infill threshold area; skirt, loop 0; extrusion width, the first layer 0%. The pre-designed structures were then printed via a Solidoodle® 3D printer platform with a nozzle size of 300 μm. Open source software (Prontrface®) was employed to control the 3 stepper motors with an effective resolution of 100 μm in the x- and y-axis, and a minimum layer height of 50 μm in the z-axis. Polyvinyl alcohol filament, with a diameter of 1.75 mm, was used as the constructing material, and the printing temperature was set at 190 °C.

2.3. Preparation of surface coating materials

The SOEA coating material was prepared based on the following procedures: briefly, 100 g SOEA was mixed with 100 ml acetone in a 500 ml brown glass bottle wrapped with two layers of aluminum foil to protect the mixture from light. Then, 1.26 g Ciba Irgacure 819 was added. The mixture was shaken mildly with hands and a 150 rpm Standard Analog Shaker (VWR International, PA, USA) alternatively to reach a homogenous yellow solution that was subsequently put into a vacuumed container overnight to remove acetone.

In addition, the PLA coating material was prepared by dissolving PLA in chloroform at concentrations of 50, 100, and 150 mg ml^{-1} until clear sticky residue observed. For the agarose coating material, agarose was dissolved in PBS in a concentration 50 mg ml^{-1}, and the mixture was preheated to 70 °C before coating. Moreover, 6.71 g castor oil, 1.68 g polycaprolactone triol (number average molecular weight of 300), and 6.61 g poly(hexamethylene diisocyanate) were mixed homogeneously in a glass beaker at room temperature in order to get the smart coating material [27].

2.4. Surface coating

The surface coater was self-established using a high-speed microcentrifuge (VWR, Radnor, PA). Briefly, a circle disc was immobilized on the centrifuge with the center of the circular disc on the rotation axis of the centrifuge and the surface of the circle disc perpendicular to the rotation axis. The FDM printed structure was fixed in the center of the circle disc. After fixing, the coating material was dripped onto the surface of the structure. The surface coating was then performed in the air while the spin speed gradually increased to 1000 rpm at which the surface coater was turned off immediately. For PCL and PLA coated structures, the samples were dried in the air for 15 min and then soaked in ethanol to remove organic solvent residuals. For SOEA coated samples, unsolidified SOEA was polymerized by putting the structure under a 355 nm wavelength UV lamp for 2 min. Agarose coated samples were immediately immersed in room temperature PBS after surface coating. After surface coating, smart material coated structures were cured at 45 °C for 72 h. The above samples were all soaked in PBS which was changed three times at 6 h intervals to completely remove polyvinyl alcohol.

2.5. Cell culture and observation

hMSCs (passage No. 3–6) were cultured in complete media composed of MEM alpha supplemented with 16.5% FBS, 1% (v/v) l-glutamine, and 1% penicillin: streptomycin solution, under standard cell culture conditions (37 °C, a humidified, 5% CO_2/95% air environment). hMSCs were seeded on the scaffolds at a cell density of 50 000 cells/ specimen and cultured under standard cell culture conditions. For observing cell morphology on the scaffold, the specimens were washed three times with PBS to remove non-adherent and dead cells. The cells were subsequently fixed with 5% formalin and permeabilized in 0.1% Triton X-100. After rinsing with PBS, the remaining cells were stained with Texas red fluorescent dye (to stain the cells' cytoskeleton) for 30 min and then DAPI blue fluorescent dye (to stain the cells' nuclei) for 15 min. The double-stained samples were imaged on a Zeiss LSM 710 confocal microscope.

When seeding cells on 3D scaffolds, a rotating bioreactor, which consists of several pieces and has a chamber to hold the scaffold and the culture media, was used. The rotating speed is 10 rpm. When seeding hMSCs on the scaffold, the scaffold and the culture media having hMSCs will be placed into the chamber of the bioreactor. The rotating bioreactor system will proceed for two days in a normal cell culture incubator.

2.6. Cell alignment quantification

The alignment of hMSCs was quantified using reported methods with slight modification [28]. Typically, the confocal images were analyzed with NIH Image J software 1.49 V (National Institutes of Health, USA). The cells were isolated from the background by setting up a threshold value of the reflection intensity. The direction of the microchannels was set as an angle of 0°. The cell major axis with respect to the direction of the microchannels was defined as the cell orientation. Cells were aligned if their angles fell into ±10° from the original benchmark.

2.7. Myogenic differentiation

The myogenic differentiation of hMSCs was performed using a reported method with modifications [29]. The hMSCs were seeded on various scaffolds at 5000 cells per cm^2 and maintained in the growth medium for two days. Myogenesis was then induced by changing the growth medium to myogenic medium, which consisted of the growth medium supplemented with 100 nM dexamethasone and 50 μM hydrocortisone. After that, the samples were cultured in the differentiation media for 14 d, and the media was exchanged every other day. At a predesigned time, the samples were collected for further biological analysis.

2.8. Immunofluorescence staining

Myogenic differentiation of hMSCs was first revealed using an immunofluorescence staining procedure. After incubation with myogenic induction medium for 7 and 14 d, the cells were washed with PBS twice and fixed with 5% cold paraformaldehyde for 10 min. The samples were treated with 0.1% Triton X-100 for 2 min and blocked in 2% BSA at room temperature for 30 min. After being washed three times with PBS, the samples were incubated in an aqueous solution of primary mouse anti-human antibodies for desmin at a dilution ratio of 1:100 in 2% BSA at 4 °C for 12 h. And then the samples were washed three times with PBS and incubated in an aqueous solution of Alexa Fluor-488 labeled goat anti-mouse IgG antibody at a dilution ratio of 1:1000 at 37 °C for 1 h. After being washed with PBS three times, the nuclei were stained with DAPI. Images of stained cells were obtained through a Zeiss LSM 710 confocal microscope.

2.9. Real-time quantitative polymerase chain reaction (rt-qPCR)

The myogenic gene expression of all samples, including myoblast differentiation protein-1 (MyoD), desmin, and myosin heavy chain-2 (MHC), were analyzed by the rt-qPCR assay. Briefly, the total RNA content was extracted from the samples using Trizol reagent. The RNA quality and concentration were determined from the absorbance at 260 and 280 nm with a microplate reader. RNA samples were reverse-transcribed to cDNA using a Prime

Script™ RT reagent Kit (TaKaRa). RT-PCR was then performed on a CFX384 Real-Time System (BIORAD) by using SYBR Premix Ex Taq™ (TaKaRa) according to the manufacturer's protocol. The gene expression level of target genes was normalized against the house keeping gene beta-actin (β-actin). The relative gene expression of the fabricated scaffold was normalized against the control group (flat PCL film) to obtain relative gene expression fold values and calculated via the 2-delta delta ($2^{-\Delta\Delta Ct}$) cycle-threshold method. Primer sequences are as follows: β-actin (NM_001101), forward primer 5′-CCCTTGCCATCCTAAAAGCC –3′ and reverse primer 5′-TGCTATCACCTCCCCTGTGT –3′; MyoD (NM_002478.4), forward primer 5′-CCGCTTTCCTTAACCACAAAT –3′ and reverse primer 5′-CGGCTGTAGATAGCAAAGTGC-3′; desmin (NM_001927.3), forward primer 5′-TCGGCTCTAAGGGCTCCTC-3′ and reverse primer 5′-CGTGGTCAGAAACTCCTGGTT-3′; MHC (NM_001100112.1), forward primer 5′-GATGGCACAGAAGTTGCTGA-3′ and reverse primer 5′-CTTCTCGTAGACGGCTTTGG-3′.

2.10. Statistical analysis

The mean and standard deviation was plotted for each sample group ($n = 6$). Then, a one-way analysis of variance (ANOVA) ($p < 0.05$) with a post-hoc Tukey Honestly Significant Difference test was performed on each set of data using GraphPad Prism (GraphPad Software Inc., California). The statistical significance was indicated with an asterisk. That is, samples marked with an asterisk were significantly different.

3. Results and discussion

3.1. Staircase morphology in FDM printing

As the PVA filament is unwound from a coil and fed through the FDM extrusion nozzle, it melts and is extruded onto a base or onto previously printed layers [24, 30]. The high-temperature PVA solidifies immediately due to the temperature difference between the nozzle (190 °C) and the room (23 °C), as well as the cooling effect from the fan. We have reported that the extruded filament does not form a perfect cylindrical strut due to the effects of gravity [27]. When we adjusted the layer height of FDM printing in the present study, the morphology of the strut was not only affected by gravity but also significantly impacted by the squeezing effect between different layers. As illustrated in figure 2(a), as we printed the scaffolds with different layer heights such as 50, 100, and 200 μm, respectively, the values of L, H and W, regarding the profile of the strut, changed accordingly. As confirmed in figure 2(b), the layer height L is very close to the theoretical value, confirming the accuracy of the printing system. Particularly, the H value is around 20 μm as the layer height is 50 and 100 μm while this value markedly increases to roughly 80 μm when the layer height is 200 μm, as shown in figure 2(c). The extruded filament was less compressed when the layer height is higher, such as 200 μm, and the arc profile of the strut is better reserved, resulting in the higher H value in figure 2(c). Similarly, the W value at the layer height of 200 μm is significantly smaller than that at layer heights of 50 and 100 μm, as shown in figure 2(d). The typical SEM images regarding this phenomenon are shown in figure 2(e). The top view (the first row) images display the strictly aligned surface of the staircases; the surface is not

well-organized when the layer height is 50 μm, compared to those with layer heights of 100 and 200 μm, but the alignment is still very clear. The side view (the second row) images reveal not only the staircase profile but also the thickness of the printed flat structure; the H value increases as the layer height increases from 50 to 200 μm; the thickness of the structure at 200 μm is clearly smaller than the thickness of those with layer heights of 50–100 μm. The images in the third row show the enlarged profiles of the staircases. These results complied with and further confirmed the results in figures 2(c) and (d). Notably, FDM has been reported to have the capacity to extrude biocompatible polymers into different size channels which provide morphological alignment and early differentiation of C2C12 cells, when cultured directly on the 3D printed scaffold [31]. However, direct fabrication of channel structures using FDM has distinct limitations. First, the channel size is determined by the width of extruded filaments; this is directly influenced by the size of commercial nozzles, which, for FDM, mostly range from 250 to 800 μm [31]. Second, as shown in figures 2(d) and (e), the thickness ($W + H$) of the scaffold from FDM is usually over 200 μm. Though this is a limitation of FDM, developing 3D constructs with very thin walls (<10 μm) is not easy for most 3D printing techniques with the exception of two photon polymerization microfabrication that can reach down to nanoscale, but is very expensive [30, 32]. While anisotropic surfaces are adequate for cell behavior regulations, the thinner the scaffold is, the less biomaterials will be present. While this may not be a critical factor for *in vitro* cell behavior regulation studies, it will be significant for *in vivo* research and potential clinical implants. Third, FDM can fabricate smart materials [33, 34], but smart FDM filaments are not widely available. To integrate smart materials with FDM, smart filaments may be custom-made, or 3D printers that are not dependent on filaments will be used. Herein, we will integrate the staircases of FDM printing with a coating technique to explore an innovative method for tissue scaffolds. Typically, staircases are controlled by layer height which is readily tunable from 50 to 200 μm in regular commercial FDM printers, and research has shown that scaffold channels in this range have a significant effect on cell behavior [22]. Surface coating is not only a well-known technique for fabricating thin structures, down to nanometers, but also a prominent approach for combining materials in a layer by layer fashion [35–37]. The combination of FDM and surface coating technique (FCT) is expected to bring new features to the realm of 3D/4D printing for the development of structures with both thin walls in three-dimensions and anisotropic surface characteristics.

3.2. FCT for anisotropic 2D scaffolds

FCT can be utilized for fabrication of different 4D transforming structures including 2D to 3D structures and 3D to 3D structures. Herein, we will first demonstrate our technique by making 2D thin film anisotropic structures with biocompatible polymers. The procedure for developing the 2D structures is illustrated in figure 3(a). The polymer solution, any of those outlined in Experimental section 2.3, was dipped directly onto the staircase surface of the FDM printed 2D structure. After surface coating and/or polymerization, the organic solvent and the PVA were removed by immersing the structure in ethanol and PBS solution sequentially. With the exception of the smart coating material, all other materials could lead to a uniform film structure using this technique. In consideration of the easy operation of PCL and its application as an implantable biomaterial, we herein will demonstrate the fabrication of 2D structures using the polymer solution of PCL in chloroform, as shown in

figures 3(b) and (c). It is very interesting that the profile of the microgroove is closely related to the concentration of PCL, as indicated in figure 3(b). At a high PCL concentration of 15%, the ridge of the microgroove is high, and the channel has an arched profile; as the PCL concentration decreases, the ridge becomes smaller and the channel nearly flattens (figure 3(b)); the profile of the microgrooves are also illustrated in figure 3(d). It is notable that the 2D anisotropic structure becomes thinner when the PCL concentration decreases. As shown in the side view in figure 3(b), the thickness of the 2D structure decreases from 10 to 1 μm as the PCL concentration decreases from 15% to 5%. When the polymer concentration is low, the polymer solution at the bottom of the staircases may fly away due to the centrifugal force of the surface coating process, resulting in the flatter channels as shown in figure 3(b). Figure 3(c) shows the microgrooves on the 2D structures with a polymer solution of 15% when the layer height is altered during FDM printing. All the microgrooves are oriented in one direction, as in figure 3(c), but it is visible that the microgrooves are not as smooth as those in figure 2(b). The rough microgrooves can be traced back to the coarse surface of the FDM printed structure. Thus, it is necessary to strictly control the conditions, starting with the FDM print, to obtain ideal anisotropic 2D microgroove structures. Although many studies have been conducted for regulating cell behavior by creating anisotropic 2D surfaces [38–43], the procedure in this study obviously provides a new and novel way to prepare anisotropic, thin, 2D scaffolds through 3D printing biomaterials.

Though cell alignment on anisotropic 2D surfaces with various microgroove morphologies has been reported, the capability of our unique 2D scaffolds for directing hMSC alignment is demonstrated. We developed the anisotropic 2D scaffolds by applying a 5% PCL solution in chloroform onto different layer height FDM printed structures, the results are shown in figure 4. Two strategies were employed to seed and culture hMSCs on the scaffolds. The first strategy is to immerse the 2D film scaffold into hMSC growth media and then add hMSC solution. As shown in figure 4(a), all the scaffolds can direct the growth of hMSCs in one direction; hMSC alignment is more pronounced at layer heights of 50 and 100 μm compared to a layer height of 200 μm, which is aligned with our previous observations [22]. The second strategy to conduct cell alignment is to immobilize the 2D film scaffold onto a ring holder which will hold the sample flat and to the bottom of the cell culture media (figure 4(b)). Figure 4(b)(i) schematically displays the sketch of the immobilized sample while figure 4(b)(ii) shows the actual sample. The white ring was FDM printed with PLA, and our sample, adhering onto the ring, is the translucent, thin, and flat anisotropic scaffold with the microgroove size of 50 μm, corresponding to the layer height of 50 μm during FDM printing. Figures 4(b)(iii)–(vi) confirms that nearly all the hMSCs aligned along the micropatterns on the 2D scaffolds, showing better morphologies than that in figures 4(a)(vii)–(ix). In our first strategy, the scaffold was floating in the cell media and the surface (figure 3 (b-5%)) is not as flat as that of the immobilized sample in the second strategy, which resulted in the different cell alignment. No matter what strategy is utilized, these results indicate that our anisotropic, thin, 2D scaffold has the capacity to effectively direct hMSC alignment, providing a new strategy for cell behavior regulation study.

3.3. FCT for 3D scaffolds with anisotropic thin wall feature

Compared to 2D anisotropic scaffolds, constructing the structures in three-dimensions would definitely provide better integration of the developed artificial scaffolds with surrounding environment for various skeletal muscle morphologies and the complex interfaces between skeletal muscles and other tissues, such as blood vessel systems or skeletons. Compared to simple 2D structures, 3D complex structures are more difficult to develop, which also demonstrates the benefit of FCT fabrication capacity and indicates greater potential for tissue regeneration. The results for the development of anisotropic 3D scaffolds are shown in figure 5. FDM is versatile for various 3D structures, such as 'ϒ' and 'ψ' shapes (figures 5(a) (i), (ii)). From left to right, the diameters of the top arms in the 'ϒ' and 'ψ' shapes are 2, 3, 4 and 5 mm, respectively, exhibiting the capabilities to print structures with different dimensions. The surface structures of these scaffolds are shown in figures 5(a)(iii)–(vi), indicating that the staircase height or the layer height is readily tunable in a range from 50 to 400 μm. During FDM printing, the layer height of the 3D printer system is very accurate as determined in figure 2(b), but it is interesting that the diameter of a printed circle by FDM is usually smaller than its theoretical value as determined in figure 5(a)(vii). During FDM printing, the extruded hot filament is dragged by the nozzle and does not solidify immediately, leading to a tendency that the filament shifts to the central point of the circle to form a smaller diameter. This phenomenon does not affect the overall structure significantly.

It should be noted that the infill density of these structures in figures 5(a)(i), (ii) is 0%, which means these structures are hollow structures, providing us more options for subsequent surface coating. We conducted the surface coating in two different ways. In the first method, we dipped different ink solutions on the outside of the FDM printed structures, as illustrated in figure 5(b)(i). After coating and removal of PVA, some typical photos of the obtained structures are shown in figures 5(b)(ii)–(iv), clearly revealing that the scaffolds were broken, owing to a sort of overexpansion. We assume that the swelling of PVA after absorption of water in PBS burst the scaffolds, which have very thin features. Figures 5(b) (v)–(vii) displays the surface features of the scaffolds, confirming that the aligned microgrooves on the surface were well preserved though the scaffold was broken. To overcome these disadvantages, we injected the polymer solution into the hollow structure of the FDM printed structures in the second method, as demonstrated in figure 5(b) (viii). The scaffolds prepared with the second method remained intact, as demonstrated in figures 5(b) (ix)–(xi), implying it is essential that the polymer solution is added inside the FDM printed structure to obtain and retain the expected anisotropic 3D structures. The complex 3D structures in figure 5 illustrated the advanced fabrication ability of the FCT strategy. These tube-like structures may not only be used for skeletal muscle tissue engineering but have great potential at the interface of muscles and blood vessels. For example, muscles could be built on the outside of tube structures while blood vessels can be built inside.

The bioreactor used to seed hMSCs on 3D scaffolds in this study is illustrated in figure 6(a). The chamber trapping the 3D scaffold is made of PDMS which is an ideal material for bioreactors because of its high gas permeability [44]. The seeding and alignment of hMSCs on a 'ϒ' anisotropic 3D scaffold are demonstrated in figure 6(b). The scaffold is prepared with PCL and shown in figures 6(b)(i), (ii). Confocal images confirm that hMSCs attached

to the surface of the scaffolds, and more importantly, the anisotropic aligned surface directed hMSC growth in the expected direction, figures 6(b)(iii)–(vi). The growth and differentiation of hMSCs on scaffolds will be further discussed in section 3.5.

3.4. FCT layer-by-layer coating for construction of 4D morphing scaffolds

4D printing is a new technology which refers to the ability of 3D printed objects to change form and/or function after fabrication, thereby offering additional capabilities and/or performance-driven applications [34]. Shape memory materials have the inherent capacity to fix a temporary shape and recover their permanent structure under suitable stimuli, which is illustrated in figure 7(a) and is extremely similar in principle with the 4D dynamic process [45–48]. 3D printing of shape memory materials is reported as novel 4D printing in recent articles, which is becoming a new, and rapidly expanding, research area in 4D printing [49–54]. Shape memory polymers have been well known for their great potential for facile and minimally invasive surgical delivery with *in situ* shape activation. This potential application provides the considerable reduction of trauma and significant improvement of patient comfort; additionally, seamless integration between the scaffold and defect would be better facilitated and addressed through the inherent shape memory effect [27, 55, 56]. Integrating shape memory polymers with FCT would result in new morphing structures, bringing this study into the realm of 4D printing.

In order to fabricate 4D scaffolds, a shape memory polymer solution was applied to coat the FDM printed structures as shown in figure 5(b)(viii). We first tested the shape memory effect of PCL to give readers a clear image that the property is significantly changed after layer by layer coating; the results are shown in figure 7(b)(i). PCL is a thermoplastic without shape memory effect, in that it cannot fix a temporary shape as illustrated in figure 7(b)(i). We then applied our thermoset shape memory polymer, which has been proved to have excellent shape memory properties and enhance the performance of hMSCs in our previous study [27], to develop smart scaffolds. However, this shape memory polymer cannot form a uniform thin film over a large area. As such, the shape memory polymer cured unevenly resulting in the misshapen structure presented in figure 7(b)(ii). Two factors are assumed to lead to the poor film-forming property of the shape memory ink. First, the shape memory ink is formulated with small molecular weight chemicals while the PCL is a long chain polymer with average Mn of 80 000. Second, the PVA, which is soluble in water and much more hydrophilic than the chemicals in the shape memory ink, hinders binding to the scaffold. It is common knowledge that thermoset polymers are mostly obtained by cross-linking smaller molecular weight chemicals compared to thermoplastic shape memory polymers. Thermoset shape memory polymers usually have superior shape memory properties compared to thermoplastics because the former have strongly covalent networks assisting in the restoration of their permanent shape. This strength of thermoset smart polymers reinforces the importance of finding an alternative way to incorporate them into our FCT scaffolds. A layer by layer process is thereafter introduced to combine our thermoset shape memory polymer with PCL-based anisotropic 3D constructs. That is, following the coating of PCL, our shape memory polymer ink was added, and further coated as depicted in figure 5(b)(viii). Our results showed that the shape memory polymer distributed evenly on the surface of the PCL and combined strongly with the PCL layer since

the polymerization of the shape memory polymer happened on the PCL layer. As shown in figure 7(c), compared to pure PCL scaffold (figure 7(b) (i)), the layer by layer structure fixed a temporary shape at $-18\ ^\circ$C with a fixed rate over 96%, and fully recovered its permanent shape at 37 $^\circ$C in the 90 s. As shown in figure 3(b) side view, the thickness of PCL layer is around 10 μm at the channel bottom where the PCL concentration is 15%, and the whole thickness, including the ridge, is 21 $\pm$ 6 μm measured with a caliper. In contrast, the thickness of the shape memory polymer layer is 49 $\pm$ 11 μm. The PCL solution has a large amount of chloroform which will evaporate after surface coating while the shape memory polymer solution is not volatile and fully cured and adhered to the PCL layer, which might contribute to the thicker shape memory layer than the PCL layer. The thickness of the shape memory polymer layer should influence the shape recovery of the layer by layer construct. As predicted, the thinner the shape memory layer is, the less the shape recovery effect is. However, in consideration of the safety and the limitation of our coating system, we used the 1000 rpm speed for all coatings and didn't increase the speed and decrease the shape memory polymer layer thickness to a critical value at which the layer by layer construct cannot recover. Beyond developing 2D layer by layer structures, we also employed this strategy to 3D structures. As shown in figures 7(d), 4D anisotropic 'ψ' scaffolds were prepared by combining PCL and our shape memory polymer layer by layer; its shape fix and recovery processes are demonstrated, indicating the versatile and robust feature of the FCT strategy for various scaffold fabrications from 2D to dynamic 4D. It is imagined that the temporary-fixed smaller scaffold can be put into the lesion position where the scaffold is going to become bigger and recover its original shape. This process has both the effect of facilitating minimally invasive procedures, and the ability to fit the scaffold properly to the surrounding tissues in view of the dynamic expanding.

3.5. The effect of topographical cues on hMSCs myogenic differentiation

One of the great advantages of 3D/4D printing is its ability to produce patient-specific scaffolds for regenerative medicine. For example, the tissue on the outer section of the deltoid muscles may need to be regenerated, not the whole deltoid. Thus, as demonstrated in figures 8(a), (b), a specific scaffold for shoulder deltoid muscle regeneration was developed, according to the native surface contour of the deltoid, and is expected to provide good integration with damaged muscle tissue. The scaffold in the figure is one-twentieth of the real muscle size, allowing us to manipulate the scaffold easily in our lab. Figure 8(c) confirms that the aligned anisotropic surface, attributed to the staircases during FDM printing, is present on the scaffolds. Thereafter, skeletal myogenic differentiation of hMSCs was performed using the developed scaffolds. We choose hMSCs for their wide range of sources, capabilities of self-renewal in an undifferentiated state for a prolonged time, and multi-lineage differentiation upon proper stimuli [57]. Via suitable biochemical inducers, hMSCs have been reported as possessing the capability to differentiate into osteocytes, chondrocytes, adipocytes, myocytes and even transdifferentiate into hepatocytes, cardiomyocytes, and neurons. Thus, our scaffolds, carrying hMSCs, possess versatile applications well beyond the coverage of the present study. Cells were seeded with the rotating bioreactor in 3.3 for two days. The developed specific scaffolds with hMSCs were then cultivated in 12 well cell plates for myogenic differentiation. This aims to demonstrate the potential patient-specific applications of our fabricated scaffolds. In addition, the shape

memory layer was not incorporated in this scaffold since the PCL layer is supposed to face hMSCs in the design. Thus, only the PCL layer was used to fabricate the scaffold as shown in figure 8. Moreover, this differentiation study also showed the unique capacity of the designed scaffold for hMSC function regulation. Usually, the channel profile for cell direction is rectangular. In contrast, our channels are complementary to the staircases on the side wall of the FDM printed structures. The ability of this type of channel to regulate cell behavior is rarely reported.

After 7 and 14 d the morphology of hMSCs and the expression of desmin were examined to determine the topographical effects of the anisotropic scaffolds. Confocal images in figures 8(d)–(g) revealed that the cells highly aligned along the direction of the microgrooves, which agrees with our previous results of cell alignment in hMSC proliferation on both 2D and 3D scaffolds. In contrast, the cell behavior on the control sample is not fully directed and is closely related to cell number. As shown in figure 8(f), the cells grew in random directions in 7 d; the cells bunched together after 14 d, as shown in figure 8(g), but had no determined direction. Additionally, the expression of desmin at 14 d is significantly higher than that at 7 d, indicating the advancement of hMSC myogenic differentiation with time.

After 14 d of incubation, RT-PCR analysis was used to determine acquired myogenic gene markers distinctive in myogenesis (figure 8(h)). The expression of MyoD, desmin, and myosin heavy chain-2 (MHC) was significantly up-regulated by about 1.5-fold in hMSCs plated on anisotropic scaffolds as compared to the negative control. While MyoD and desmin are biomarkers of skeletal myogenic lineages at the early stage, MHC is expressed in myogenic precursors undergoing terminal differentiation [58–62]. The significantly increased expression of MyoD, desmin, and MHC in differentiated hMSCs indicated the progressive myogenic lineage development of hMSCs. It has been reported that aligned nanofibers can provide topographical cues to induce cell alignment with a potential effect on expression of genes indicative of myogenic induction of hMSCs cultured in a proliferative and non-differentiating medium, but upregulation of desmin was not observed [10]. In contrast, the topographical cues in our study are significantly different, and biochemical inducers, dexamethasone, and hydrocortisone, were applied, which may have contributed to the differing results. In another reported work, micro/nano-hybrid patterns were constructed by establishing micro-stripes with different spacings (50, 100 and 200 μm) on polystyrene nano-grooves, where the direction of the micro-stripes and nano-grooves was parallel or orthogonal; while the myogenic induction medium was supplied with 1 ng ml^{-1} transforming growth factor β1, differentiation of hMSCs on these structures showed that myogenic differentiation was predominantly regulated by cell alignment [63], which is aligned with our results, though different biochemical inducers were used. In addition to hMSCs, it has also been reported that differentiation of other cell lines, such as human embryonic stem cells, can be significantly enhanced by exposure to aligned topological cues [64]. Both studies cited previously, and our results herein, suggest that aligned anisotropic topographical cues affect and regulate cell behaviors enhancing myogenic differentiation.

4. Conclusion

The staircase defect present in FDM printing can be harnessed as an effective strategy for fabricating anisotropic structures from 2D to 4D with great potential for skeletal muscle tissue engineering applications. By optimizing polymer concentrations, adjusting FDM printing layer height, and applying a suitable coating approach, versatile surface morphologies can be prepared which provide topographical cues for directing hMSC alignment and enhancing myogenic differentiation. Through layer-by-layer surface coating, shape memory polymer was readily integrated into the fabricated structures, providing shape change features and taking this research into the field of 4D printing. With many other natural tissues and organs also having highly organized and structurally anisotropic components, such as myocardium, vessel, and neural tissues, the FCT strategy explored in the present study possesses wide application potential in tissue engineering.

Acknowledgments

Abbreviations

DAPI	4′,6 - Diamidino - 2 - phenylindole, dihydrochloride
FCT	FDM and coating technique
FDM	fused deposition modeling
hMSCs	human mesenchymal stem cells
MHC	myosin heavy chain-2
MyoD	differentiation protein-1
PBS	phosphate-buffered saline
PCL	polycaprolactone
PLA	poly lactic acid
PVA	polyvinyl alcohol
RT-PCR	transcription polymerase chain reaction analysis
SOEA	soybean oil epoxidized acrylate

References

[1]. Vigodarzere GC and Mantero S 2014 Skeletal muscle tissue engineering: strategies for volumetric constructs Front. Physiol 5 362 [PubMed: 25295011]

[2]. Hamilton B, Valle X, Rodas G, Til L, Grive RP, Rincon JAG and Tol JL 2015 Classification and grading of muscle injuries: a narrative review Br. J. Sports Med 49 306–306 [PubMed: 25394420]

[3]. Turner NJ and Badylak SF 2012 Regeneration of skeletal muscle Cell Tissue Res 347 759–74 [PubMed: 21667167]

[4]. Manring H, Abreu E, Brotto L, Weisleder N and Brotto M 2014 Novel excitation-contraction coupling related genes reveal aspects of muscle weakness beyond atrophy—new hopes for treatment of musculoskeletal diseases Front. Physiol 5 37 [PubMed: 24600395]

[5]. Jana S, Levengood SKL and Zhang M 2016 Anisotropic materials for skeletal-muscle-tissue engineering Adv. Mater 28 10588–612 [PubMed: 27865007]

[6]. Choi Y-J, Park SJ, Yi H-G, Lee H, Kim DS and Cho D-W 2018 Muscle-derived extracellular matrix on sinusoidal wavy surfaces synergistically promotes myogenic differentiation and maturation J. Mater. Chem B 6 5530–9

[7]. Liu J, Saul D, Böker KO, Ernst J, Lehman W and Schilling AF 2018 Current methods for skeletal muscle tissue repair and regeneration BioMed Res. Int 2018 1984879

[8]. Kuraitis D, Giordano C, Ruel M, Musarò A and Suuronen EJ 2012 Exploiting extracellular matrix-stem cell interactions: a review of natural materials for therapeutic muscle regeneration Biomaterials 33 428–43 [PubMed: 22014942]

[9]. Sato M, Ito A, Kawabe Y, Nagamori E and Kamihira M 2011 Enhanced contractile force generation by artificial skeletal muscle tissues using IGF-I gene-engineered myoblast cells J. Biosci. Bioeng 112 273–8 [PubMed: 21646045]

[10]. Dang JM and Leong KW 2007 Myogenic induction of aligned mesenchymal stem cell sheets by culture on thermally responsive electrospun nanofibers Adv. Mater 19 2775–9 [PubMed: 18584057]

[11]. Jahani H, Jalilian FA, Wu CY, Kaviani S, Soleimani M, Abassi N, Ou KL and Hosseinkhani H 2015 Controlled surface morphology and hydrophilicity of polycaprolactone toward selective differentiation of mesenchymal stem cells to neural like cells J. Biomed. Mater. Res A 103 1875–81

[12]. Yang F, Murugan R, Wang S and Ramakrishna S 2005 Electrospinning of nano/micro scale poly (L-lactic acid) aligned fibers and their potential in neural tissue engineering Biomaterials 26 2603–10 [PubMed: 15585263]

[13]. Lim SH, Liu XY, Song H, Yarema KJ and Mao H-Q 2010 The effect of nanofiber-guided cell alignment on the preferential differentiation of neural stem cells Biomaterials 31 9031–9 [PubMed: 20797783]

[14]. Kim J, Staunton JR and Tanner K 2016 Independent control of topography for 3D patterning of the ECM microenvironment Adv. Mater 28 132–7 [PubMed: 26551393]

[15]. Wang Z-Y, Teo EY, Chong MSK, Zhang Q-Y, Lim J, Zhang Z-Y, Hong M-H, Thian E-S, Chan JKY and Teoh S-H 2013 Biomimetic three-dimensional anisotropic geometries by uniaxial stretch of poly (ɛ-caprolactone) films for mesenchymal stem cell proliferation, alignment, and myogenic differentiation Tissue Eng C 19 538–49

[16]. Wang ZY, Lim J, Ho YS, Zhang QY, Chong MS, Tang M, Hong MH, Chan JK, Teoh SH and Thian ES 2014 Biomimetic three-dimensional anisotropic geometries by uniaxial stretching of poly (ɛ-caprolactone) films: degradation and mesenchymal stem cell responses J. Biomed. Mater. Res A 102 2197–207

[17]. Wang Z-Y, Teoh SH, Johana NB, Chong MSK, Teo EY, Hong M-H, Chan JKY and San Thian E 2014 Enhancing mesenchymal stem cell response using uniaxially stretched poly (ɛ-caprolactone) film micropatterns for vascular tissue engineering application J. Mater. Chem B 2 5898–909

[18]. Béduer A, Vieu C, Arnauduc F, Sol J-C, Loubinoux I and Vaysse L 2012 Engineering of adult human neural stem cells differentiation through surface micropatterning Biomaterials 33 504–14 [PubMed: 22014459]

[19]. Hsu S, Su CH and Chiu IM 2009 A novel approach to align adult neural stem cells on micropatterned conduits for peripheral nerve regeneration: a feasibility study Artif. Organs 33 26–35 [PubMed: 19178438]

[20]. Bhuthalingam R, Lim PQ, Irvine SA, Agrawal A, Mhaisalkar PS, An J, Chua CK and Venkatraman S 2015 A novel 3D printing method for cell alignment and differentiation Int. J. Bioprinting 1 57–65

[21]. Barry RA, Shepherd RF, Hanson JN, Nuzzo RG, Wiltzius P and Lewis JA 2009 Direct-write assembly of 3D hydrogel scaffolds for guided cell growth Adv. Mater 21 2407–10

[22]. Miao S, Cui H, Nowicki M, Lee S-J, Almeida J, Zhou X, Zhu W, Yao X, Masood F and Plesniak MW 2018 Photolithographic-stereolithographic-tandem fabrication of 4D smart scaffolds for improved stem cell cardiomyogenic differentiation Biofabrication 10 035007

[23]. Zein I, Hutmacher DW, Tan KC and Teoh SH 2002 Fused deposition modeling of novel scaffold architectures for tissue engineering applications Biomaterials 23 1169–85 [PubMed: 11791921]

[24]. Yang E, Miao S, Zhong J, Zhang Z, Mills DK and Zhang LG 2018 Bio-based polymers for 3D printing of bioscaffolds Polym. Rev 58 668–87

[25]. Gross BC, Erkal JL, Lockwood SY, Chen C and Spence DM 2014 Evaluation of 3D printing and its potential impact on biotechnology and the chemical sciences Anal. Chem 86 3240–53 [PubMed: 24432804]

[26]. He Y, Xue G-H and Fu J-Z 2014 Fabrication of low cost soft tissue prostheses with the desktop 3D printer Sci. Rep 4 6973 [PubMed: 25427880]

[27]. Miao S, Zhu W, Castro NJ, Leng J and Zhang LG 2016 Four-dimensional printing hierarchy scaffolds with highly biocompatible smart polymers for tissue engineering applications Tissue Eng C 22 952–63

[28]. Lanfer B, Seib FP, Freudenberg U, Stamov D, Bley T, Bornhäuser M and Werner C 2009 The growth and differentiation of mesenchymal stem and progenitor cells cultured on aligned collagen matrices Biomaterials 30 5950–8 [PubMed: 19674785]

[29]. Zhao C, Andersen H, Ozyilmaz B, Ramaprabhu S, Pastorin G and Ho HK 2015 Spontaneous and specific myogenic differentiation of human mesenchymal stem cells on polyethylene glycol-linked multi-walled carbon nanotube films for skeletal muscle engineering Nanoscale 7 18239–49 [PubMed: 26486984]

[30]. Ngo TD, Kashani A, Imbalzano G, Nguyen KT and Hui D 2018 Additive manufacturing (3D printing): a review of materials, methods, applications and challenges Composites B 143 172–96

[31]. Rimington RP, Capel AJ, Christie SD and Lewis MP 2017 Biocompatible 3D printed polymers via fused deposition modelling direct C2C12 cellular phenotype in vitro Lab Chip 17 2982–93 [PubMed: 28762415]

[32]. Xing J-F, Zheng M-L and Duan X-M 2015 Two-photon polymerization microfabrication of hydrogels: an advanced 3D printing technology for tissue engineering and drug delivery Chem. Soc. Rev 44 5031–9 [PubMed: 25992492]

[33]. Yang H, Leow WR, Wang T, Wang J, Yu J, He K, Qi D, Wan C and Chen X 2017 3D printed photoresponsive devices based on shape memory composites Adv. Mater 29 1701627

[34]. Miao S, Castro N, Nowicki M, Xia L, Cui H, Zhou X, Zhu W, Lee S-J, Sarkar K and Vozzi G 2017 4D printing of polymeric materials for tissue and organ regeneration Mater Today 20 577–91

[35]. Richardson JJ, Björnmalm M and Caruso F 2015 Technology-driven layer-by-layer assembly of nanofilms Science 348 aaa2491 [PubMed: 25908826]

[36]. Lee S-S, Hong J-D, Kim CH, Kim K, Koo JP and Lee K-B 2001 Layer-by-layer deposited multilayer assemblies of ionene-type polyelectrolytes based on the spin-coating method Macromolecules 34 5358–60

[37]. Jiang C, Markutsya S and Tsukruk VV 2004 Compliant, robust, and truly nanoscale free-standing multilayer films fabricated using spin-assisted layer-by-layer assembly Adv. Mater 16 157–61

[38]. Li Y, Huang G, Zhang X, Wang L, Du Y, Lu TJ and Xu F 2014 Engineering cell alignment in vitro Biotechnol. Adv 32 347–65 [PubMed: 24269848]

[39]. Anene-Nzelu CG, Peh KY, Fraiszudeen A, Kuan YH, Ng SH, Toh YC, Leo HL and Yu H 2013 Scalable alignment of three-dimensional cellular constructs in a microfluidic chip Lab Chip 13 4124–33 [PubMed: 23969512]

[40]. Zhang D, Xu S, Wu S and Gao C 2018 Micropatterned poly (d, l-lactide-co-caprolactone) films entrapped with gelatin for promoting the alignment and directional migration of Schwann cells J. Mater. Chem B 6 1226–37

[41]. Hu J, Hardy C, Chen C-M, Yang S, Voloshin AS and Liu Y 2014 Enhanced cell adhesion and alignment on micro-wavy patterned surfaces PLoS One 9 e104502 [PubMed: 25105589]

[42]. Chew SY, Mi R, Hoke A and Leong KW 2008 The effect of the alignment of electrospun fibrous scaffolds on Schwann cell maturation Biomaterials 29 653–61 [PubMed: 17983651]

[43]. Takahashi H, Shimizu T, Nakayama M, Yamato M and Okano T 2013 The use of anisotropic cell sheets to control orientation during the self-organization of 3D muscle tissue Biomaterials 34 7372–80 [PubMed: 23849343]

[44]. Leclerc E, Sakai Y and Fujii T 2004 Microfluidic PDMS (polydimethylsiloxane) bioreactor for large-scale culture of hepatocytes Biotechnol. Prog 20 750–5 [PubMed: 15176878]

[45]. Zhao Q, Qi HJ and Xie T 2015 Recent progress in shape memory polymer: new behavior, enabling materials, and mechanistic understanding Prog. Polym. Sci 49 79–120

[46]. Hager MD, Bode S, Weber C and Schubert US 2015 Shape memory polymers: past, present and future developments Prog. Polym. Sci 49 3–33

[47]. Miao S, Callow N, Wang P, Liu Y, Su Z and Zhang S 2013 Soybean oil-based polyurethane networks: shape-memory effects and surface morphologies J. Am. Oil Chem. Soc 90 1415–21

[48]. Miao S, Wang P, Su Z, Liu Y and Zhang S 2012 Soybean oil-based shape-memory polyurethanes: synthesis and characterization Eur. J. Lipid Sci. Technol 114 1345–51

[49]. Zhou Y, Huang WM, Kang SF, Wu XL, Lu HB, Fu J and Cui H 2015 From 3D to 4D printing: approaches and typical applications J. Mech. Sci. Technol 29 4281–8

[50]. Pei E 2014 4D Printing: dawn of an emerging technology cycle Assem. Autom 34 310–4

[51]. Huang L, Jiang R, Wu J, Song J, Bai H, Li B, Zhao Q and Xie T 2016 Ultrafast digital printing toward 4D shape changing materials Adv. Mater 29 1605390

[52]. Miao S, Zhu W, Castro NJ, Nowicki M, Zhou X, Cui H, Fisher JP and Zhang LG 2016 4D printing smart biomedical scaffolds with novel soybean oil epoxidized acrylate Sci. Rep 6 27226 [PubMed: 27251982]

[53]. Zarek M, Layani M, Eliazar S, Mansour N, Cooperstein I, Shukrun E, Szlar A, Cohn D and Magdassi S 2016 4D printing shape memory polymers for dynamic jewellery and fashionwear Virtual Phys. Prototyp 11 263–70

[54]. Miao S, Cui H, Nowicki M, Xia L, Zhou X, Lee SJ, Zhu W, Sarkar K, Zhang Z and Zhang LG 2018 Stereolithographic 4D bioprinting of multiresponsive architectures for neural engineering Adv. Biosyst 2 1800101

[55]. Zhang D, George OJ, Petersen KM, Jimenez-Vergara AC, Hahn MS and Grunlan MA 2014 A bioactive 'self-fitting' shape memory polymer scaffold with potential to treat cranio-maxillo facial bone defects Acta Biomater 10 4597–605 [PubMed: 25063999]

[56]. Machado L and Savi M 2003 Medical applications of shape memory alloys Braz. J. Med. Biol. Res 36 683–91 [PubMed: 12792695]

[57]. Zhao C, Tan A, Pastorin G and Ho HK 2013 Nanomaterial scaffolds for stem cell proliferation and differentiation in tissue engineering Biotechnol. Adv 31 654–68 [PubMed: 22902273]

[58]. Sartorelli V and Caretti G 2005 Mechanisms underlying the transcriptional regulation of skeletal myogenesis Curr. Opin. Genet. Dev 15 528–35 [PubMed: 16055324]

[59]. Blais A, Tsikitis M, Acosta-Alvear D, Sharan R, Kluger Y and Dynlacht BD 2005 An initial blueprint for myogenic differentiation Gene. Dev 19 553–69 [PubMed: 15706034]

[60]. Stewart JD, Masi TL, Cumming AE, Molnar GM, Wentworth BM, Sampath K, McPherson JM and Yaeger PC 2003 Characterization of proliferating human skeletal muscle-derived cells in vitro: differential modulation of myoblast markers by TGF-β2 J. Cell. Physiol 196 70–8 [PubMed: 12767042]

[61]. Beier JP, Bitto FF, Lange C, Klumpp D, Arkudas A, Bleiziffer O, Boos AM, Horch RE and Kneser U 2011 Myogenic differentiation of mesenchymal stem cells co-cultured with primary myoblasts Cell Biol. Int 35 397–406 [PubMed: 20946104]

[62]. Gang EJ, Jeong JA, Hong SH, Hwang SH, Kim SW, Yang IH, Ahn C, Han H and Kim H 2004 Skeletal myogenic differentiation of mesenchymal stem cells isolated from human umbilical cord blood Stem Cells 22 617–24 [PubMed: 15277707]

[63]. Yang Y, Wang X, Huang T-C, Hu X, Kawazoe N, Tsai W-B, Yang Y and Chen G 2018 Regulation of mesenchymal stem cell functions by micro–nano hybrid patterned surfaces J. Mater. Chem B 6 5424–34

[64]. Leung M, Cooper A, Jana S, Tsao C-T, Petrie TA and Zhang M 2013 Nanofiber-based in vitro system for high myogenic differentiation of human embryonic stem cells Biomacromolecules 14 4207–16 [PubMed: 24131307]
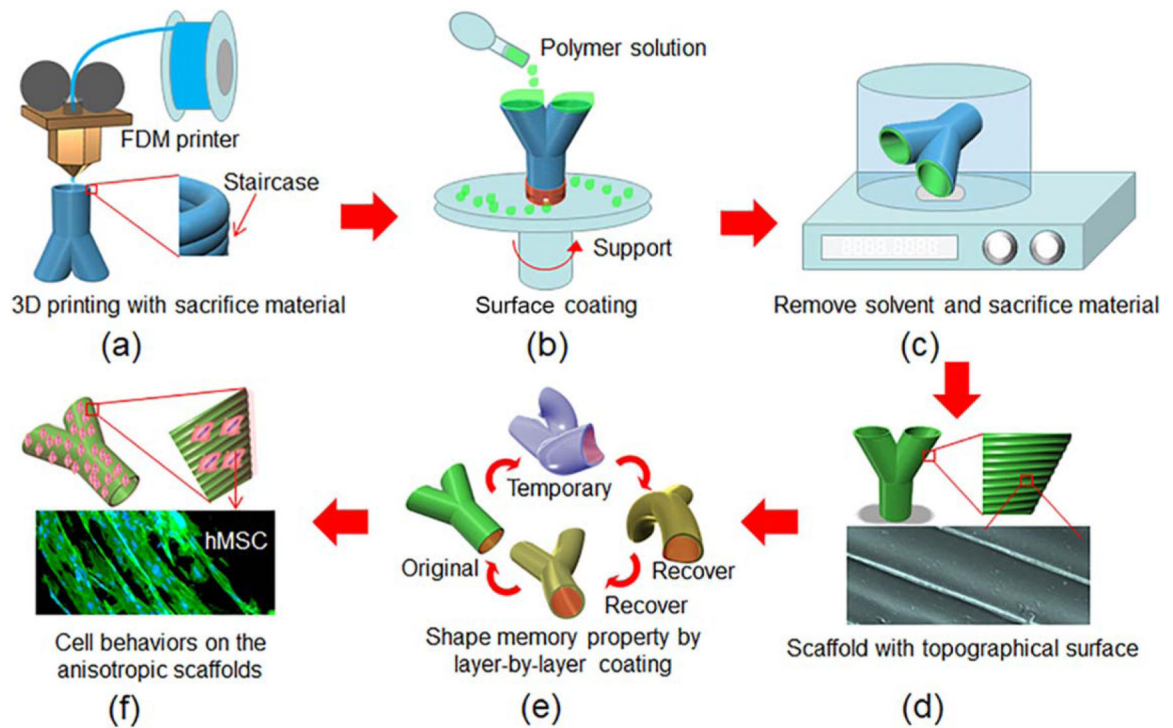
Figure 1.
Illustration of the fabrication process for development of shape-specific anisotropic scaffold using the FDM and surface coating technique (FCT). (a) FDM printed pre-designed structures with staircases on surface. (b) Surface coating with different polymer solutions to develop thin films on the structures. (c) The organic solvent residuals from polymer solution and the sacrifice materials are removed. (d) The 3D scaffolds with specific surface morphologies. (e) Shape memory property after layer-by-layer coating with shape memory polymer. (f) Investigate cell behaviors on the scaffolds.
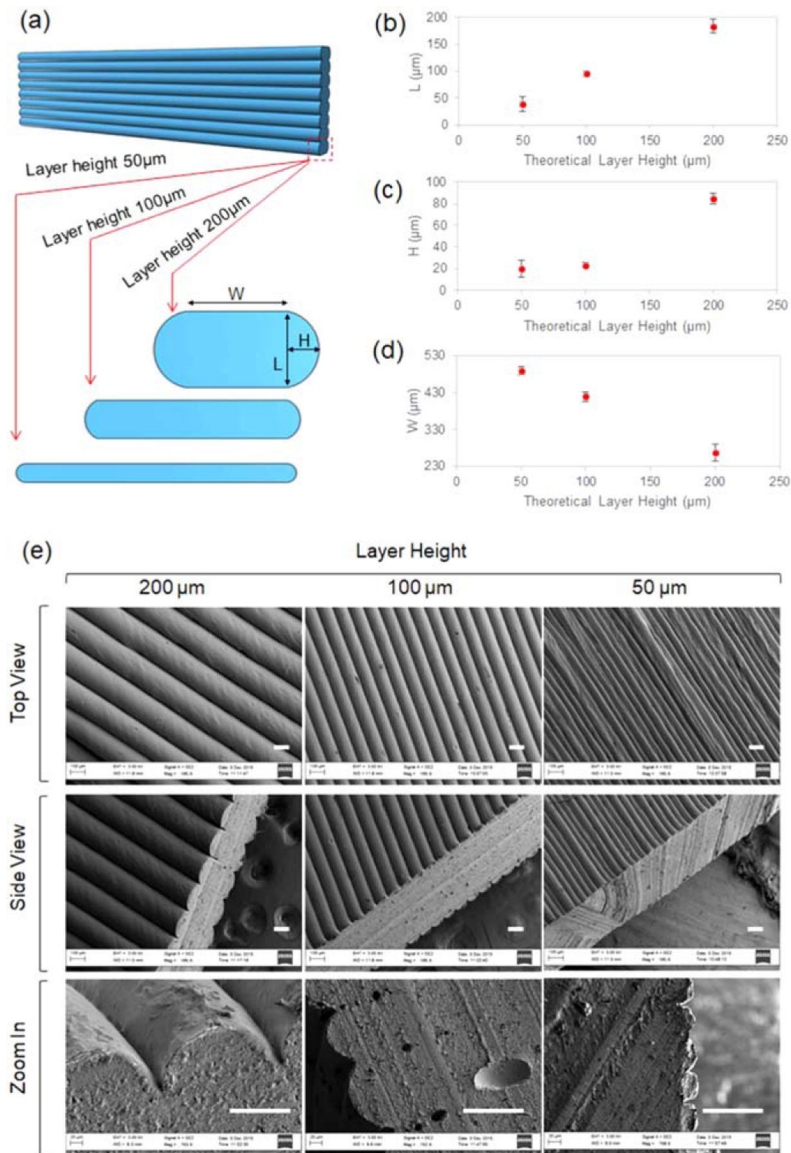
Figure 2.
The staircase morphology of FDM printing. (a) The illustration of the profile of the struts at different layer height. (b) The *L* value at different layer height. (c) The *H* value at different layer height. (d) The *W* value at different layer height. (e) SEM images of the staircases in FDM printing. Scale bar 100 μm.
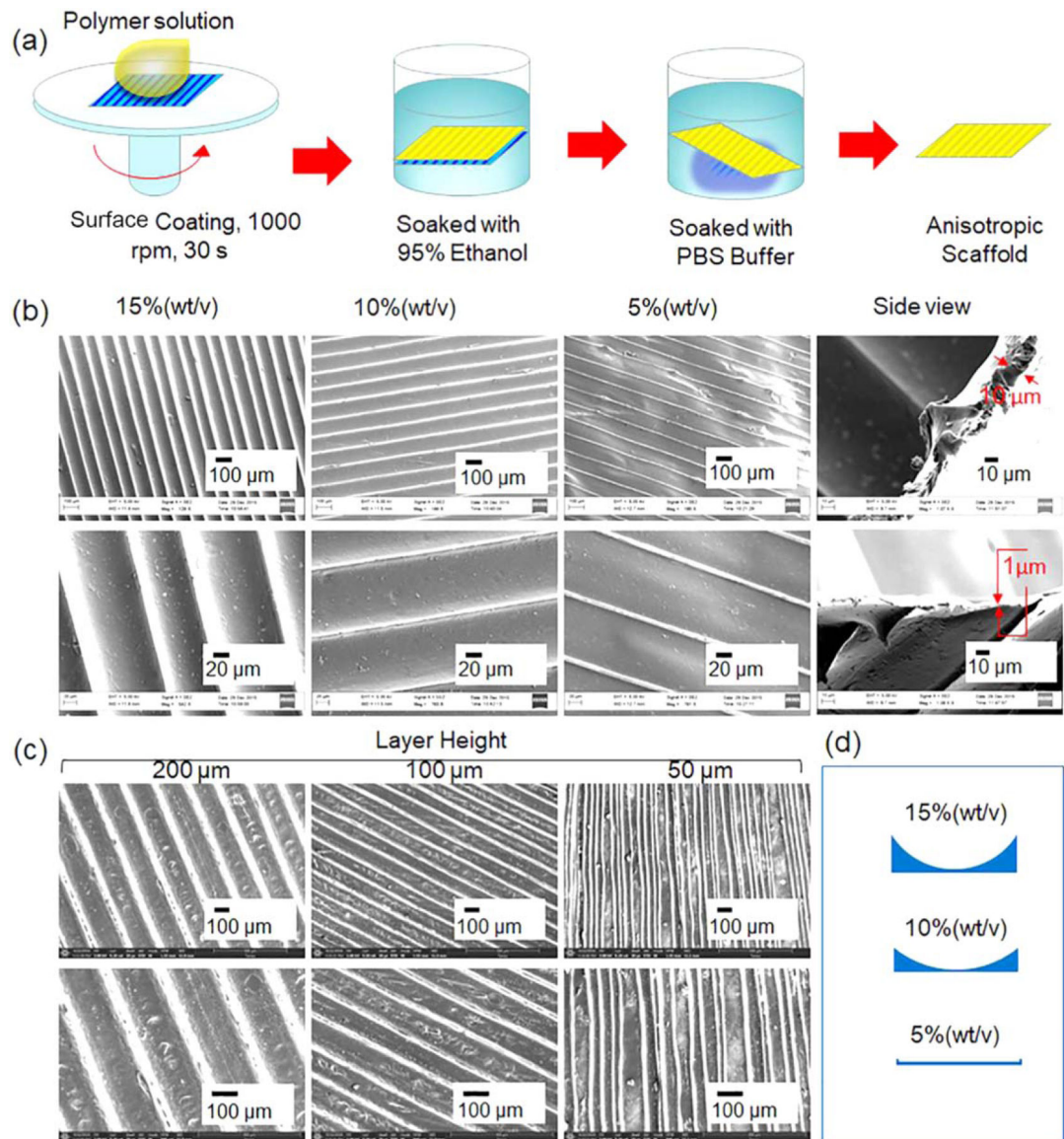
Figure 3.
FCT fabrication of 2D structures. (a) The procedure for preparing the 2D thin scaffold with anisotropic surface feature. (b) The SEM images of the 2D scaffolds developed using the FDM structures at layer height of 100 μm with different polymer concentrations of PCL in chloroform. 1% (wt/v) refers to 1 g PCL in 100 ml chloroform. The upper image in side view is the profile of the 2D structure at the polymer concentration of 15%. The lower image is at the polymer concentration of 5%. (c) The SEM images of the 2D scaffolds fabricated via FDM structures with different layer height using the polymer solution of 15%. (d) The illustration is of the profiles of the microgrooves as the polymer concentration varies.
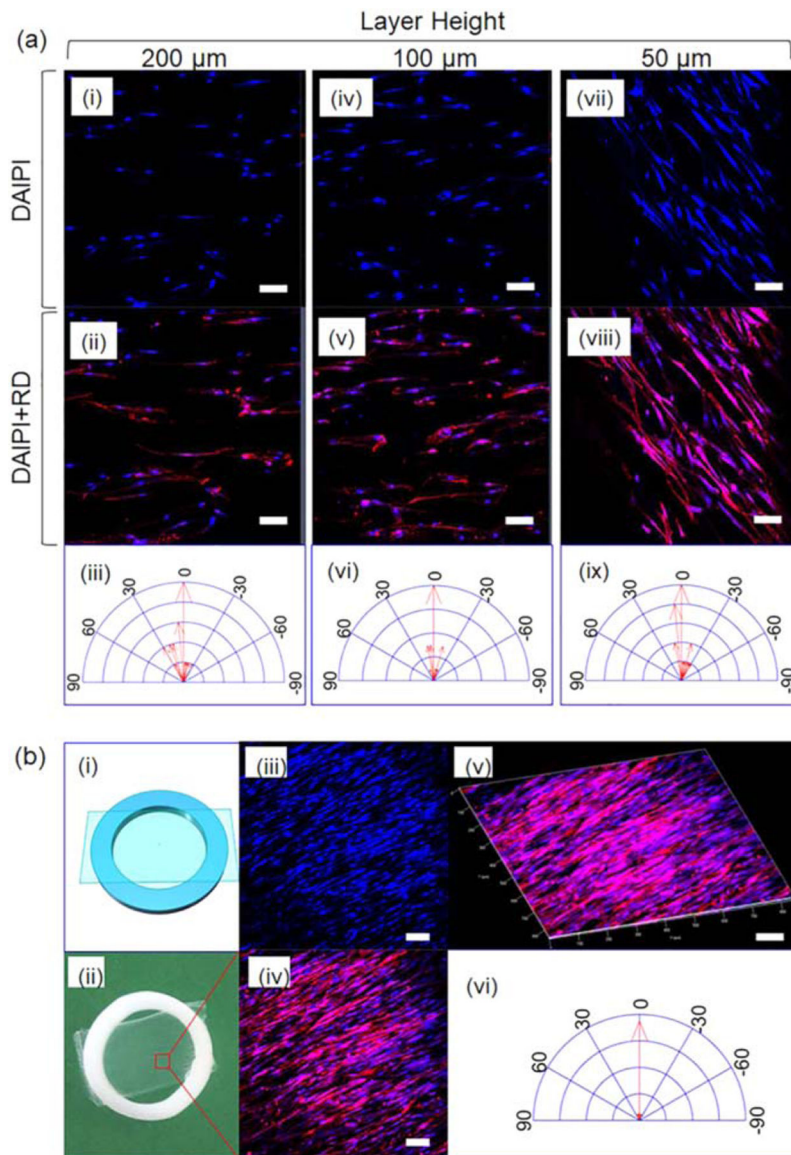
Figure 4.
hMSCs alignment on anisotropic 2D thin scaffolds. (a) The morphology of hMSC on the 2D scaffolds with varied microgroove width. The 2D scaffolds were immersed in the cell media before cell seeding without immobilization. (b) The morphology of hMSCs on the 2D scaffold with 50 μm microgroove width developed with 5% PCL in chloroform. The scaffold was immobilized on a PLA ring which holds the sample flat and static during cell seeding and growth. Scale bar, 100 μm.
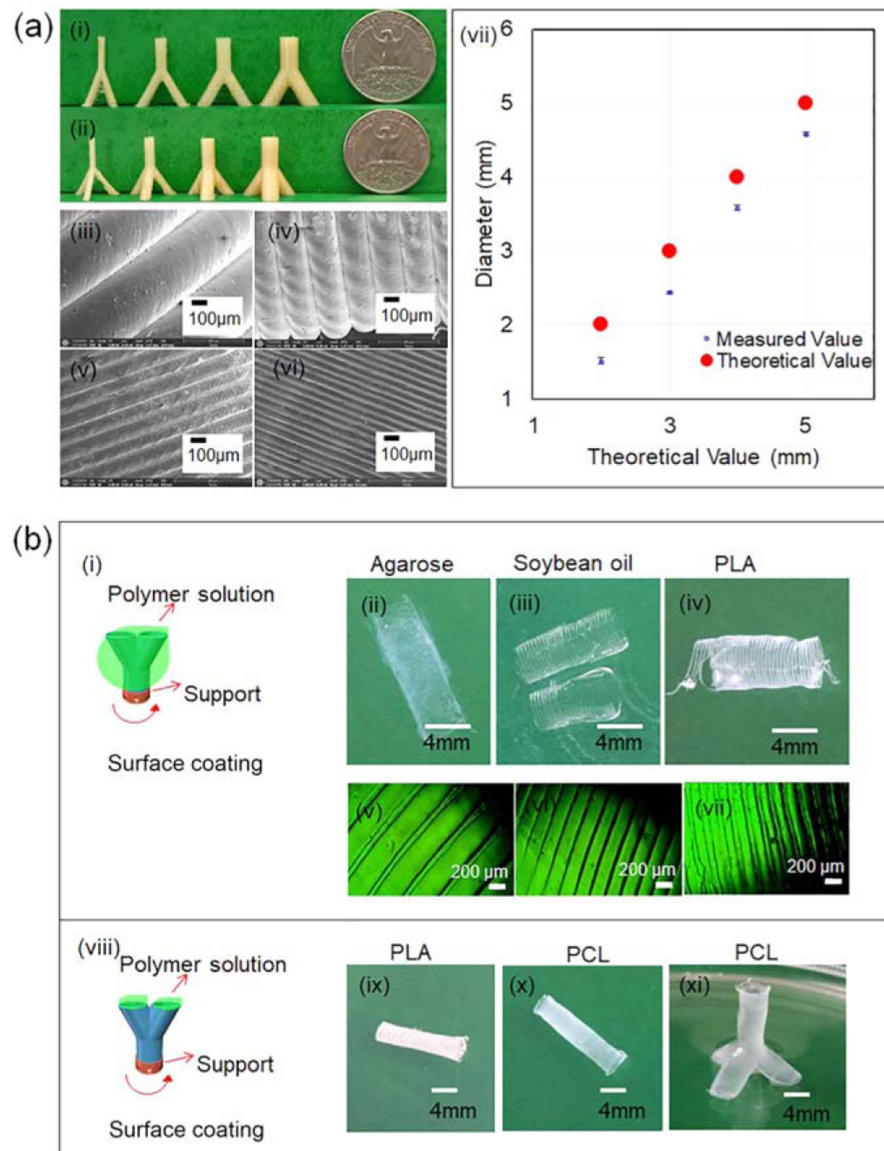
Figure 5.
(a) FDM printed 3D structure. (i), (ii) Photo of the structures. (iii)–(vi) SEM images of the surface structures. (vii) The plot of theoretical diameter versus measured diameter. (b) Surface coating strategies. (i) Coat polymers on the outside surface of the structure. (ii)–(iv) Photos of the scaffolds. (v)–(vii) Surface structures of corresponding scaffolds. (viii) Coat inside polymer. (ix)–(xi) Photos of the scaffolds.
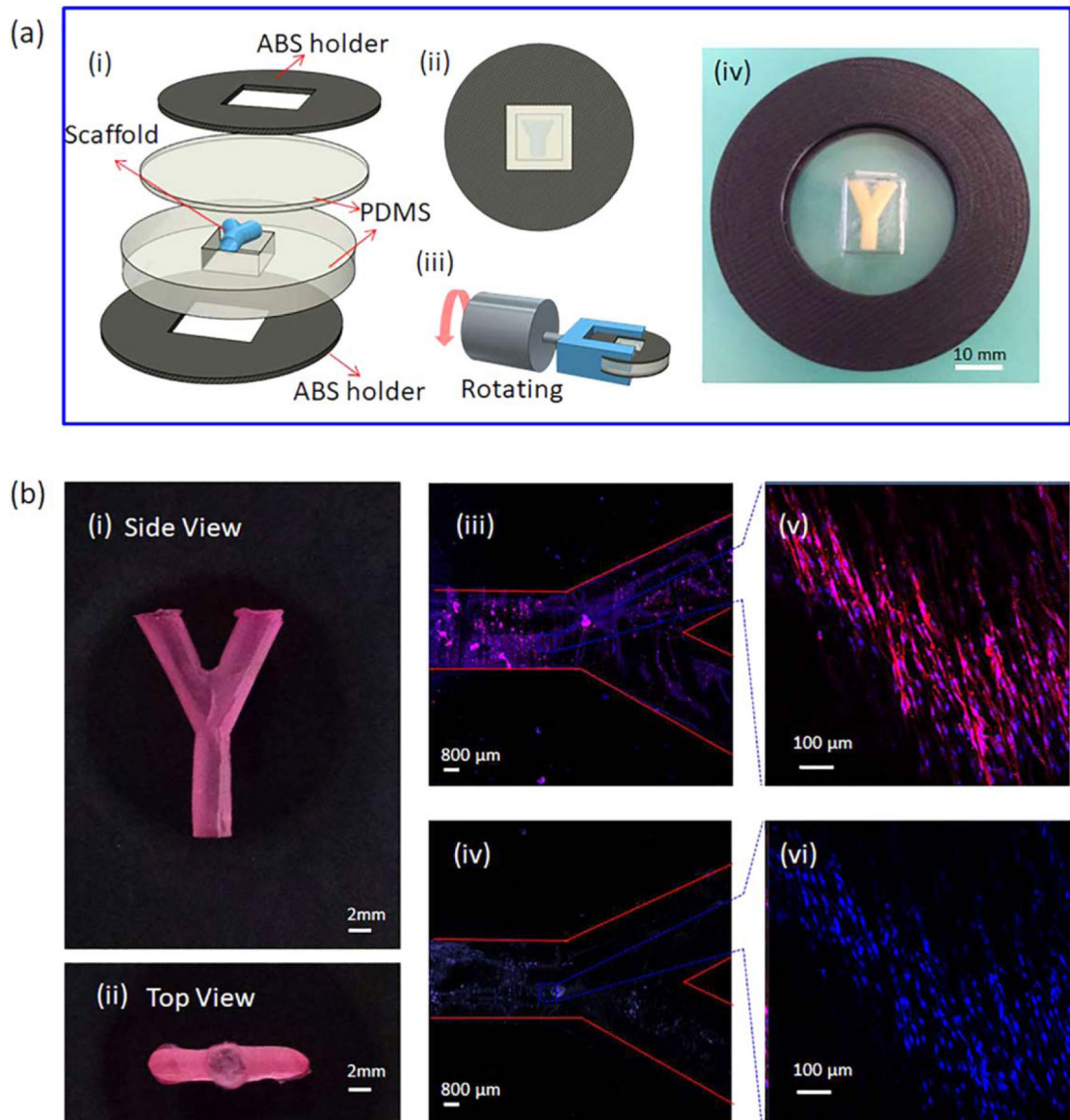
Figure 6.
Cell seeding onto the anisotropic 3D scaffolds using self-established bioreactor. (a) Schematic design of the bioreactor. (i) Separated pieces of the bioreactor. (ii) The bioreactor after assembly. (iii) The bioreactor is immobilized on a rotator. (iv) The photo of the real bioreactor. (b) The scaffold before and after cell seeding. (i) Side view of the scaffold stained with 0.01% Nile red. (ii) Top view of the scaffold. (iii), (vi) Confocal images of hMSCs stained with Texas red and DAPI, respectively. (v), (vi) Confocal images of spots on the scaffold confirming the alignment of hMSCs.
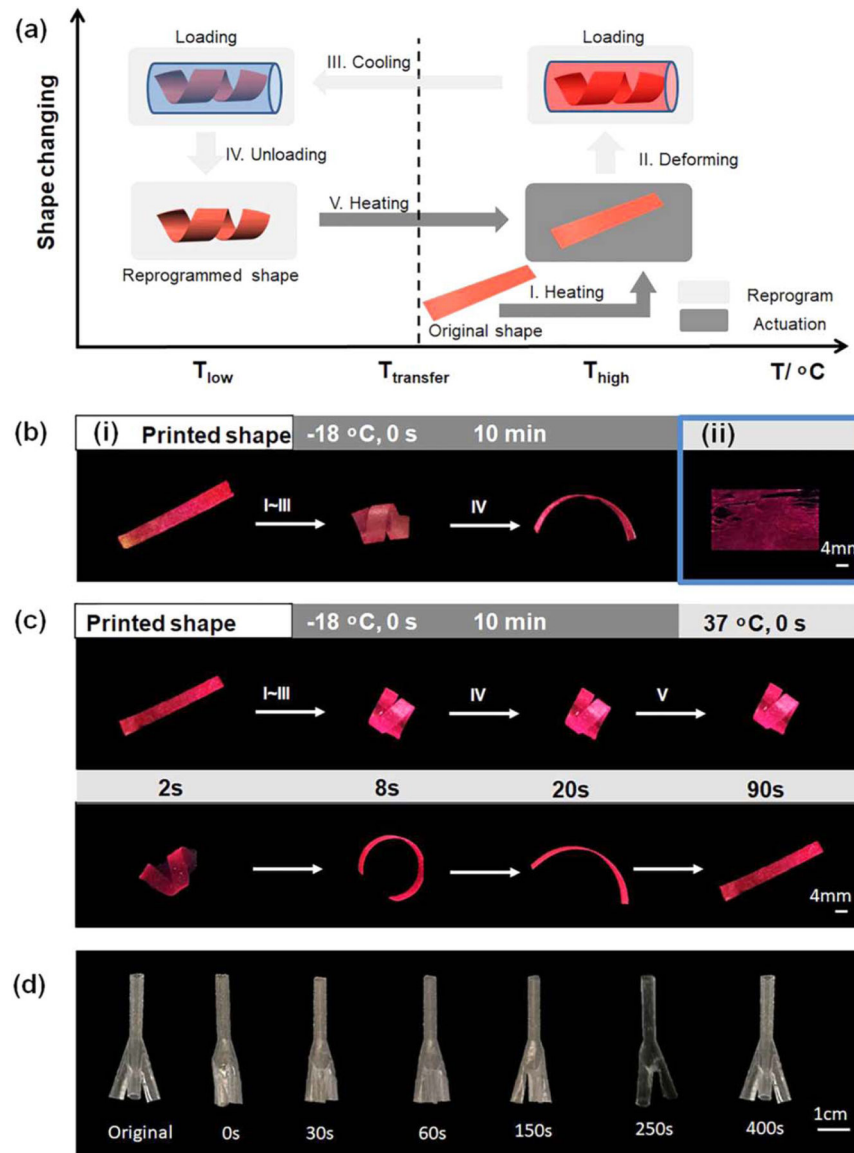
Figure 7.
Shape memory property of fabricated scaffolds. (a) Illustration of the process of shape memory effect. (b) (i) PCL scaffold's original shape and fixity. (ii) Defect is observed on pure shape memory polymer-based scaffolds. (c) Shape memory property of PCL-shape memory polymer scaffold. (d) Shape recovery process of 3D scaffold.
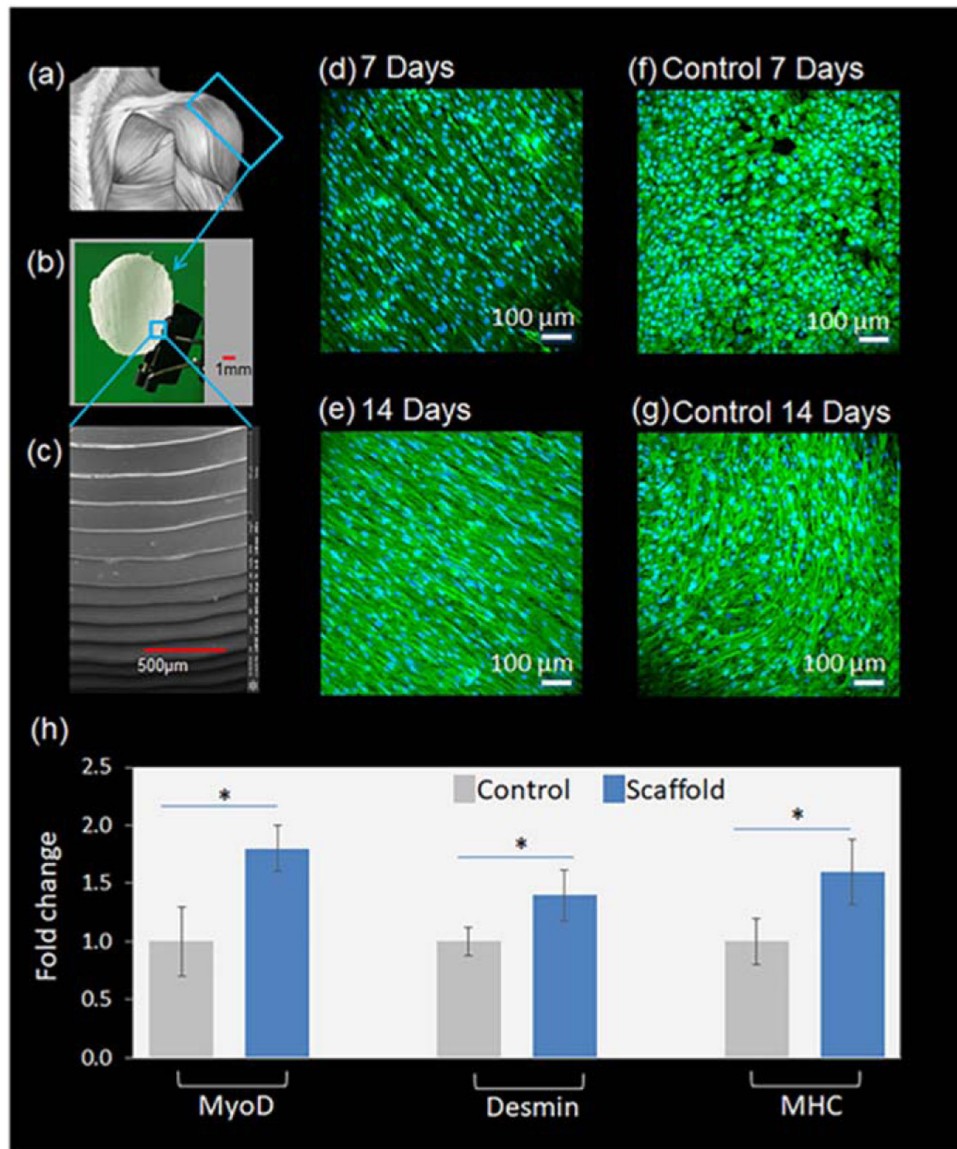
Figure 8.

The effect of topographical cues on hMSC myogenic differentiation. (a)–(c) Fabrication of patient-specific scaffold using PCL. (d)–(g) Desmin immunofluorescence staining of 4D scaffolds and PCL control samples (PCL flat films) on 7 and 14 d, respectively. (h) Myogenic gene expression on 14 d determined by RT-PCR analysis. *$P < 0.05$.